Localized Exciton Anatomy and BandGap Energy Modulation in 1D MoS$_2$ Nanostructures

van der Lippe, Stijn; Brokkelkamp, Abel; Rojo, Juan; Conesa-Boj, Sonia

Important note
To cite this publication, please use the final published version (if applicable).
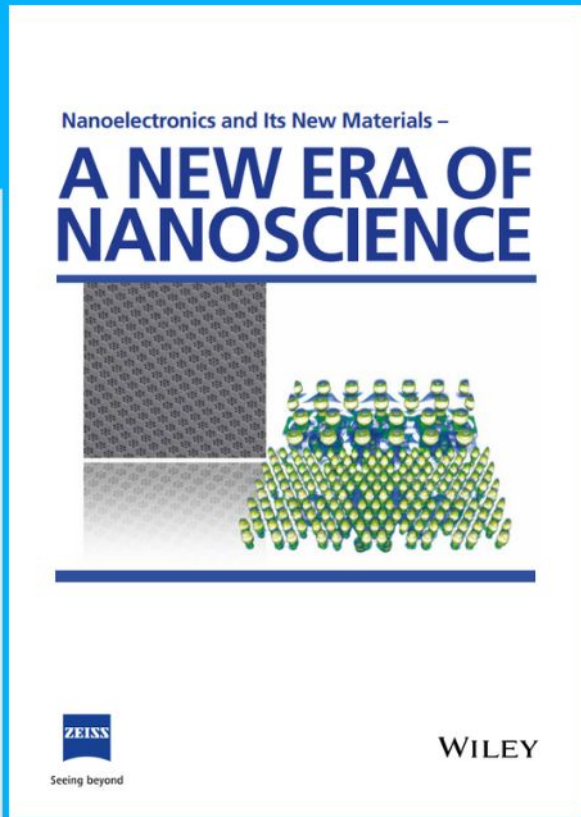Please check the document version above.

Nanoelectronics and Its New Materials – A NEW ERA OF NANOSCIENCE

Discover the recent advances in electronics research and fundamental nanoscience.

Nanotechnology has become the driving force behind breakthroughs in engineering, materials science, physics, chemistry, and biological sciences. In this compendium, we delve into a wide range of novel applications that highlight recent advances in electronics research and fundamental nanoscience. From surface analysis and defect detection to tailored optical functionality and transparent nanowire electrodes, this eBook covers key topics that will revolutionize the future of electronics.

To get your hands on this valuable resource and unleash the power of nanotechnology, simply download the eBook now. Stay ahead of the curve and embrace the future of electronics with nanoscience as your guide.

Localized Exciton Anatomy and BandGap Energy Modulation in 1D MoS$_2$ Nanostructures

*Stijn van der Lippe, Abel Brokkelkamp, Juan Rojo, and Sonia Conesa-Boj**

This study presents an in-depth investigation of the electronic properties and bandgap energy distribution in 1D molybdenum disulfide (1D-MoS$_2$) nanostructures. Through a combination of high-angle annular dark-field scanning transmission electron microscopy (HAADF-STEM) and electron energy-loss spectroscopy (EELS), it reveals significant differences between 1D-MoS$_2$ nanostructures and their 2D counterparts, shedding light on their localized exciton behavior and their bandgap energy modulation within the nanostructures. Excitonic peaks at around 2 and 3 eV appear localized at the ends or along the sides of the 1D-MoS$_2$ nanostructures, while the plasmonic resonance at 8.3 eV retains its inner-region localization. It demonstrates the spatial dependence of the bandgap energy, with the central region exhibiting a bandgap of approximately 1.2 eV, consistent with bulk MoS$_2$, while regions characterized by curvature-induced local strain fields exhibit instead a noticeable reduction. The findings provide valuable insights into the intricate relationship between excitonic behavior and bandgap sensitivity in 1D-MoS$_2$ nanostructures, streamlining the design and optimization of nanophotonic and optoelectronic devices.

1. Introduction

2D van der Waals materials, both in the traditional planar configuration as well as in their 1D counterpart, have captivated substantial interest due to their remarkable electrical and optical properties. Transition metal dichalcogenides, particularly

molybdenum disulfide (MoS$_2$), have emerged as leading candidates for next-generation nanoelectronics and optoelectronics due to their inherent semiconducting nature. Central to the optical functionalities of MoS$_2$ are excitons, electron-hole bound states whose behavior can be modified by means of localization arising from potential minima[1] induced by defects,[2,3] strain,[4,5] or local potential variations.[6] In recent years, extensive research has focused on investigating the electronic and optical properties of 2D-MoS$_2$ nanostructures. These materials offer indeed unique opportunities for tailoring their properties through spatial localization and manipulation of excitonic resonances. In this context, the study of 1D-MoS$_2$ nanostructures holds tremendous potential for unlocking novel possibilities in customization and design complementing those provided by the planar configuration. Understanding these properties is crucial for the design and optimization of nanoscale devices in applications to nanoelectronics and optoelectronics.

Localized excitons in TMD-based nanostructures exhibit strikingly different behaviors compared to their free counterparts, directly impacting the resulting optoelectronic functionalities. For instance, their longer lifetimes[7] and narrower photoluminescence linewidths[8] make them highly appealing for applications such as single-photon emitters,[9,10] which in turn are crucial for future quantum technologies like quantum optics[11,12] and quantum networking.[13,14]

The unique platform provided by 1D-MoS$_2$ nanostructures is expected to allow the hosting of localized excitons through curvature-induced quantum confinement. However, a comprehensive understanding of the properties of these localized excitons in 1D-MoS$_2$ remains so far elusive. A challenge of this configuration is the possible presence of several confounding effects, including strain fields and structural defects, which may alter the optoelectronic properties such as the bandgap and the location and intensity of localized excitonic transitions.

In this study, we undertake a thorough investigation of localized excitons in 1D-MoS$_2$ nanostructures, complemented by the assessment of their bandgap energy modulation. This is achieved by leveraging and extending our previously developed approach[15,16] for the automated processing and interpretation of electron energy-loss spectroscopy (EELS) spectral images (SI)

S. van der Lippe, A. Brokkelkamp, S. Conesa-Boj
Kavli Institute of Nanoscience
Delft University of Technology
Delft 2628 CJ, The Netherlands
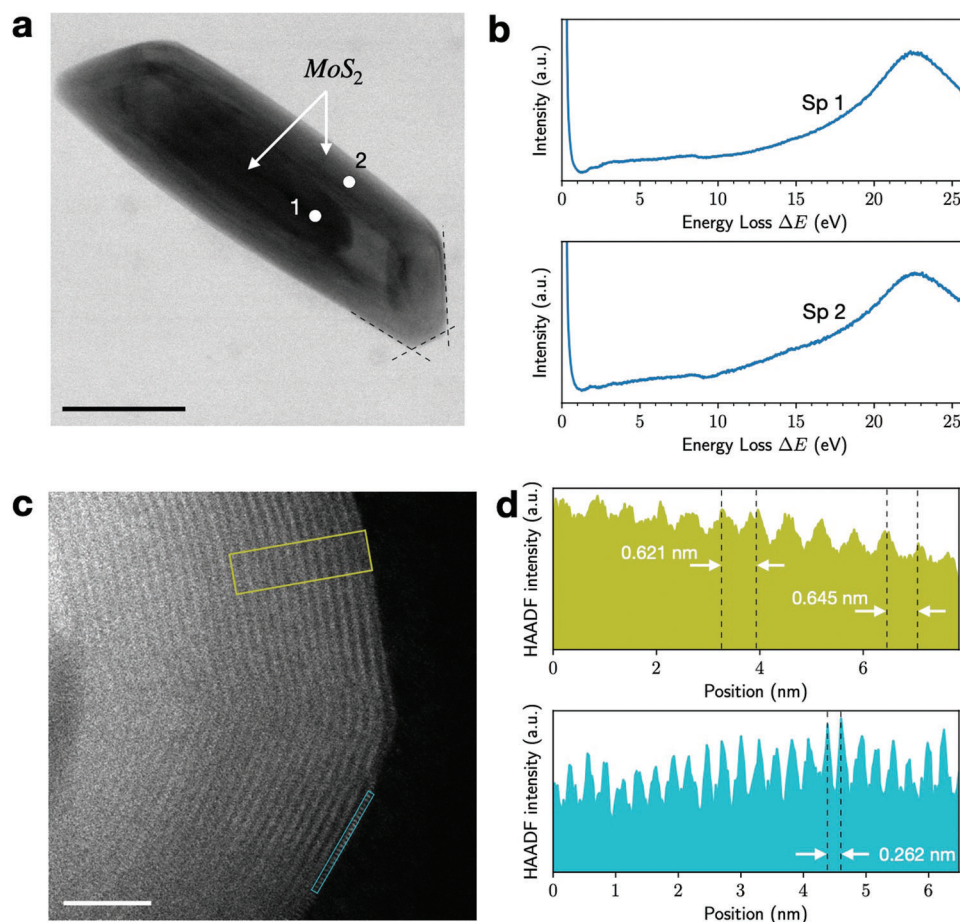E-mail: s.conesaboj@tudelft.nl
J. Rojo
Nikhef Theory Group
Science Park 105, Amsterdam 1098 XG, The Netherlands
J. Rojo
Department of Physics and Astronomy
VU, Amsterdam 1081 HV, The Netherlands

The ORCID identification number(s) for the author(s) of this article can be found under https://doi.org/10.1002/adfm.202307610

Figure 1. Morphology of the 1D-MoS_2 nanostructures. a) Bright-field image of a representative 1D-MoS_2 nanostructure. The size of the scale bar is 50 nm. b) High-resolution EEL spectra corresponding to the regions indicated in a) and displaying the MoS_2 bulk plasmon peak at 22.5 eV. c) High-resolution HAADF-STEM image of the tip of the same 1D-MoS_2 nanostructure. The size of the scale bar is now 5 nm. d) Line scans acquired in the regions marked in (c) with green and blue rectangles. The top line scan identifies the separation between atomic planes to be approximately 0.63 nm, while the inter-atomic distance is determined to be around 0.262 nm from the bottom line scan. The line scan origin corresponds to the left-most end of the marked regions.

with nanometer spatial resolution implemented within the open-source EELSFITTER framework. We identify several excitonic transitions and plasmonic resonances in 1D-MoS_2 nanostructures, echoing previous findings in the 2D-MoS_2 case. We demonstrate the localization of the excitonic peaks around 2 and 3 eV at the ends or along the sides of the nanostructures, while the plasmonic resonance at 8.3 eV retains its inner-region localization.

The spatially-resolved analysis of bandgap energy reveals an indirect bandgap in all specimens studied. We identify specific trends between bandgap energy modulation and structural features attributed to the presence of curvature-induced local strain fields. In particular, while the central region of the specimens displays a bandgap of around 1.2 eV, consistent with bulk MoS_2, regions displaying tensile strain, such as the endpoints, exhibit instead a reduction with respect to the bulk value.
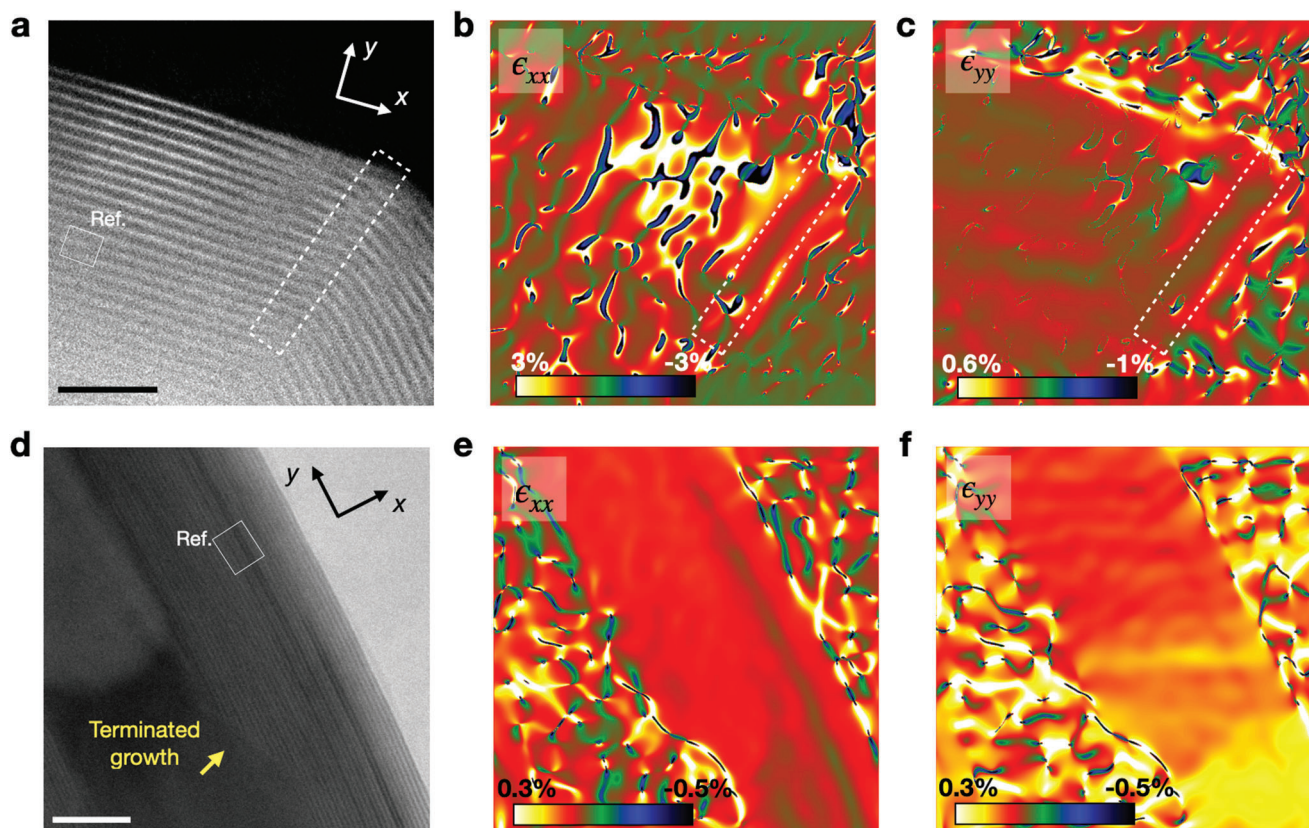
Our insights into the intricate relationship between excitonic behavior and bandgap variability in 1D-MoS_2 nanostructures bear significant implications for the future engineering of nanophotonic and optoelectronic devices. By comprehending the spatial configuration-dependent electronic properties of these

nanostructures, we can effectively design and optimize nanoscale devices, resulting in enhanced performance and advancements in applications in these fields.

2. Results and Discussion

The 1D-MoS_2 nanostructures investigated in this work were synthesized by means of chemical vapor deposition (CVD) techniques.[17] They were directly grown on a 5 nm thick Si_3N_4 membrane spanning the Transmission Electron Microscopy (TEM) grid. More details on the growth methodology can be found in the Experimental Section.

The synthesized nanostructures exhibit a characteristic core-shell structure, as illustrated in the bright-field TEM image of **Figure 1**a. Confirmation of the presence of MoS_2 in both the core and the shell regions was achieved by acquiring EELS at two distinct positions within the nanostructure, Figure 1b, displaying the plasmon peak located at 22.5 eV consistent with previous studies.[18–22] Further evidence is provided in Figure 1d with line profiles extracted from the high-resolution high-angle annular

**ADVANCED
SCIENCE NEWS**

www.advancedsciencenews.com

**ADVANCED
FUNCTIONAL
MATERIALS**

www.afm-journal.de

Figure 2. Strain analysis of 1D-MoS$_2$ nanostructures. a) HAADF-STEM image of a region located around the bend region of the tip of a 1D-MoS$_2$ nanostructure. The size of the scale bar is 5 nm. b,c) The strain components ϵ_{xx} and ϵ_{yy} extracted by means of GPA from (a), revealing the presence of tensile strain peaking at 0.45 % near the bend with a decrease at the point of maximum bending. This tensile strain is associated with the presence of structural defects. d) High-resolution TEM image of a region along the length of the nanostructure close to the tip, displaying terminated growth of the inner layers of the 1D-MoS$_2$ nanostructures leading to variations in wall thickness and diameter along this length. The size of the scale bar is 10 nm. e,f) Strain components ϵ_{xx} and ϵ_{yy} extracted by means of GPA from (d). Tensile strain is observed along the length, which gradually increases as the shell thickness varies. The reference regions for strain calculation are indicated with a white solid rectangle in (a) and (d).

dark-field scanning transmission electron microscopy (HAADF-STEM) image of the tip of the same 1D-MoS$_2$ nanostructure (Figure 1c). The distances between the peaks in the line profile provides information on the interlayer spacing, which is found to be approximately 6 Å and consistent with the interlayer distance of MoS$_2$ reported in the literature.[23] We also observe that as we move closer to the outer layer of the nanostructure, this interlayer distance increases. Upon closer examination of the nanostructure's edge, we observe bright spots (indicated with a blue rectangle in Figure 1c) indicating atomic contrast arising from Mo atoms. To determine the Mo–Mo distance, we also conducted a line profile analysis finding the expected separation of approximately 0.262 nm.

The 1D-MoS$_2$ nanostructures considered in this work are showcased in Figure S1 (Supporting Information) and exhibit an average length and diameter of 960 and 60 nm, respectively. Their close examination reveals several interesting features. In particular, the rolling up of the MoS$_2$ sheets along the MoS$_2$ core leads to the formation of tubular structures, which display distinctive faceted caps at their tips (see Figure 1a, with dashed lines highlighting these features) that should induce the formation of localized tensile strain.

To quantify the strain distribution within the 1D-MoS$_2$ nanostructures, we employ the Geometrical Phase Analysis (GPA) method.[24,25] **Figure 2** presents the GPA strain analysis of two representative regions of the 1D-MoS$_2$ nanostructure, one located near the maximum bending point in the tip and providing insight into the strain distribution in a highly curved region, while the other is positioned along the length of the nanostructure and allowing us to examine strain variations in a relatively straight section. In the vicinity of the maximum bending point, the MoS$_2$ layers are found to exhibit tensile strain, with values reaching up to 0.45 % (Figures 2b,c) with respect to the reference region for the diagonal components ϵ_{xx} and ϵ_{yy}. Interestingly, strain is comparatively lower at the precise maximum bending region, marked by a dashed white rectangle in Figure 2a, and which also reveals the presence of structural defects in the form of discontinuous layers in this region. The observed decrease in strain at the maximum bending point, accompanied by the presence of structural defects, can be attributed to the inherent requirements for the MoS$_2$ layers to satisfy stacking order and orientation relationship with respect to the previous layer. The strain involved in the formation of these 1D-MoS$_2$ nanostructures, specially at their pronounced tips, is therefore relaxed through the formation

**ADVANCED
SCIENCE NEWS**
www.advancedsciencenews.com

**ADVANCED
FUNCTIONAL
MATERIALS**
www.afm-journal.de

of structural defects. The type of defects identified in Figure 2a correspond to basal plane dislocations, which in turn can lead to twin defects.[26] The formation of the latter in 2D materials minimizes the total energy by balancing the strain energy caused by lattice distortion with the van der Waals energy between neighboring planes.

Furthermore, one observes that the inner layers of the 1D-MoS$_2$ nanostructure considered exhibit terminated growth (marked by an arrow in Figure 2d). This results in variations in the wall thickness on the two sides of the 1D-MoS$_2$ nanostructures and leads to a varying diameter of the shell along the length of the nanostructure (see Figure S1, Supporting Information). This type of terminated growth has been previously reported in metallic-filled carbon nanotubes[27] and in WS$_2$ nanotubes.[28] Strain is also observed along the length of the 1D-MoS$_2$ nanostructures, as quantified by the ϵ_{xx} and ϵ_{yy} maps in Figure 2e, f. In particular, we find tensile strain which gradually increases as the shell thickness varies.

As shown in Figure S2 (Supporting Information), our growth strategy also results in alternative morphologies for the 1D-MoS$_2$ nanostructures, and in particular a fraction of them are connected by their end regions. In the subsequent analysis, we consider both a individual 1D-MoS$_2$ nanostructure as well as joint pair of nanostructure. The presence of bent layers, varying diameters, and interconnected arrangements in these nanostructures has associated the potential to modulate their local electronic properties, as we demonstrate in the following.

2.1. Spatially-Resolved STEM-EELS Characterization

The morphological and structural features of 1D-MoS$_2$ nanostructures reported in Figures 1 and 2 motivate the in-depth analysis of their local optoelectronic properties. To this end, we conduct EELS measurements on individual nanostructures to identify and study collective electronic excitations, such as excitons and plasmons, and to determine their bandgap energy. Our focus is primarily the low-loss region, with energy losses $\Delta E \leqslant 50$ eV, providing direct insights into the sought-for excitonic and plasmonic behavior. This analysis builds upon the open-source EELSFITTER framework[15,16] for the processing of spatially-resolved EELS data, here extended with automated peak-tracking algorithms.
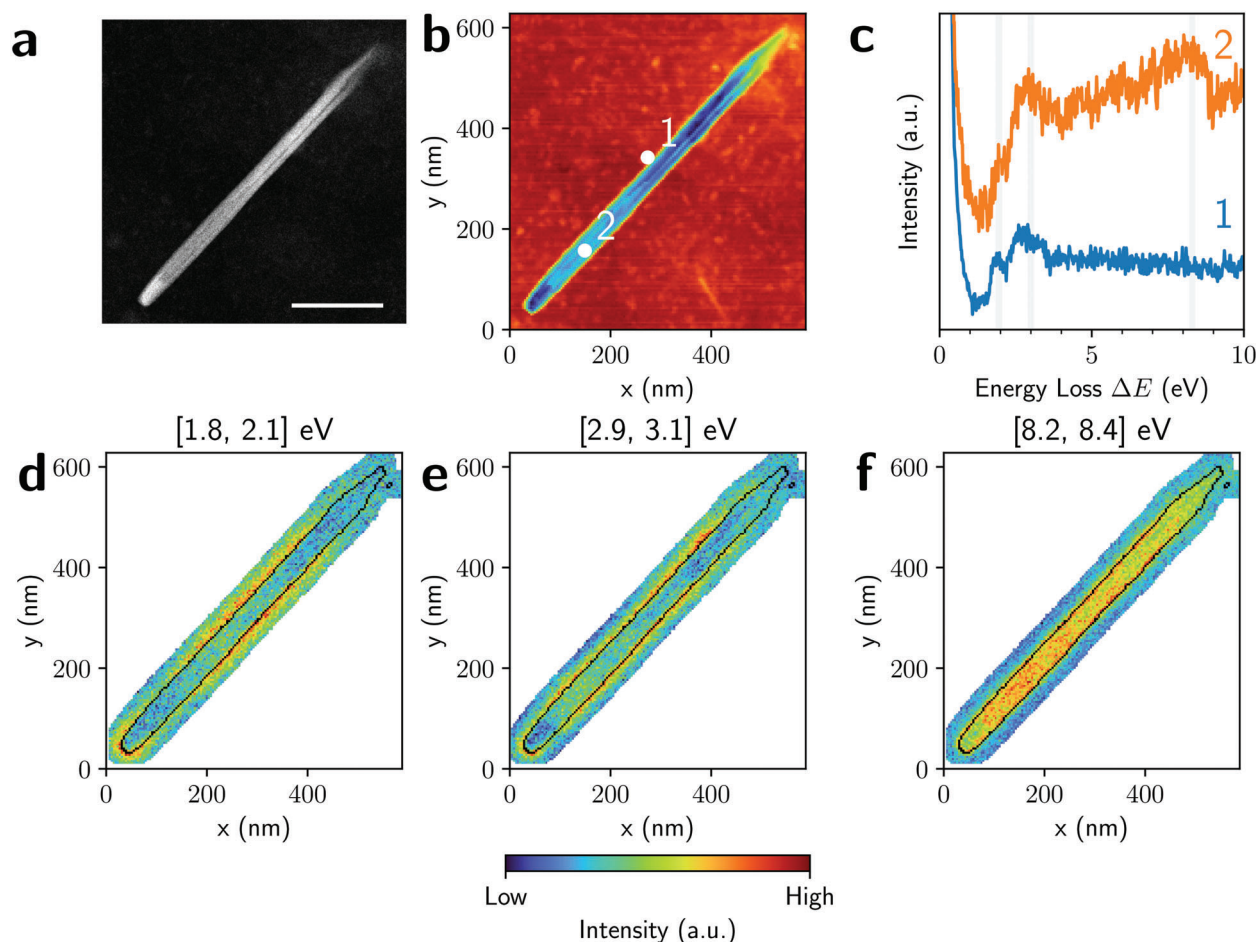
Figure 3a displays a HAADF-STEM image of a representative 1D-MoS$_2$ nanostructure. Figure 3b displays the EELS spectral image acquired on this specimen, where the color map corresponds to the total integrated intensity per pixel. In Figure 3c, individual EEL spectra acquired at two distinct positions on the nanostructure (indicated in Figure 3b) are shown. In order to reduce statistical noise, spectra are pooled using a 3×3 mask. They are also normalized to a common factor and offset in the vertical direction to facilitate visualization. The highlighted spectra exhibit significant variations between the two positions in the specimen, one close to the surface (spectrum 1, sp1 for short) and another toward the center (sp2). Specifically, sp1 (surface) displays prominent peak-like features at energies of around 1.9 and 3.0 eV, while sp2 (central region) exhibits instead localized intensity enhancements around 3.0 and 8.3 eV.

In order to investigate the spatial dependence of the observed features across the nanostructure, we determine specific energy intervals over which the EELS intensity is integrated following the procedure described in Section S2 (Supporting Information). This strategy is based on an automated peak-finding algorithm identifying resonant features in EELS-SI spectra, complemented by manual inspection. Figure 3d–f display the resulting integrated intensity maps corresponding to the ranges of [1.8,2.1] , [2.9,3.1] , and [8.2,8.4] eV, respectively. We focus on the region of the spectral image containing the nanostructure, delineated by the black curve indicating its boundary, and we filter out the substrate region and the rest of the spectral image. Note that each panel adopts a different intensity range.

The spatially-resolved EELS analysis of Figure 3d–f illustrates how the peak-like features reported in the individual spectra of Figure 3c vary across the 1D-MoS$_2$ nanostructure. In the energy-loss range of [1.8,2.1] eV, the strongest signal intensity is observed at one of the tips of the nanostructure as well as along the sides, specially in the central region. For the energy-loss range of [2.9,3.1] eV, the signal is most marked along the sides of the nanostructure, with a moderate enhancement observed at one of the tips as well. In the [8.2,8.4] eV energy-loss range, the intensity is mostly enhanced along half of the length of the nanostructure, excluding the tip regions. It has been reported[29] that for MoS$_2$ the peaks at 8.3 eV appear only for non-zero momentum q. Overall, one finds that the energy value and intensity of several peak-like features in the EELS spectra vary sensitively with respect to the spatial location within the nanostructure.

Figure 4 then presents a similar analysis as that of Figure 3 now for a different morphology: two 1D-MoS$_2$ nanostructures connected by their endpoints, as demonstrated by the HAADF-STEM analysis presented in Figure S2 (Supporting Information) and in particular by the HAADF-STEM image of Figure S2a (Supporting Information). With the aim of identifying the implications of this interconnected configuration, Figure 4b displays three representative spectra taken at different locations in the specimen, again exhibiting distinctive features depending on the location. Marked peak-like intensity enhancements at around 1.7 eV (sp1), 2.0 eV (sp2) and at both 2.7 eV and 8.3 eV (sp3) respectively are observed. The integrated intensity maps shown in Figures 4c–f indicate that these intensity enhancements are localized in the range [1.6, 1.8] eV at the tips of the bottom nanostructure, along the edge in the middle region of the top nanostructure for [1.9, 2.1] eV, at the middle parts of the nanostructures as well as at the region where the nanostructures are connected for [2.6, 2.8] eV, and at the inner part of the nanostructures for the [8.2, 8.4] eV energy-loss range. The reproducibility of this analysis is confirmed by the results in Section S3 (Supporting Information), corresponding to another connected specimen with a similar morphology. The intensity enhancement around 1.7 eV, absent for the nanostructure in Figure 3, can be ascribed to strain effects shifting the exciton peak at 2 eV to smaller energies.

The energies of some of the observed peak-like intensity enhancements in the analyzed 1D-MoS$_2$ nanostructures align closely with values reported in the literature for 2D MoS$_2$ specimens based on theoretical calculations,[30] EELS measurements,[29,31,32] and photoluminiscence studies.[33] Specifically, the peaks located around 2 and 3 eV can be explained as arising from excitonic transitions, while the peak

**ADVANCED
SCIENCE NEWS**

www.advancedsciencenews.com

**ADVANCED
FUNCTIONAL
MATERIALS**

www.afm-journal.de

Figure 3. Spatially-resolved EELS analysis of a 1D-MoS$_2$ nanostructure. a) HAADF-STEM image of a MoS$_2$ nanostructure with a length of 760 nm and a diameter of 40 nm. The size of the scale bar is 200 nm. b) The corresponding EELS-SI, where the color map corresponds to the total integrated intensity per pixel. c) Representative spectra associated to the pixels indicated in (b). These spectra exhibit intensity enhancements at specific energies and are offset in the vertical direction for clarity. d–(f) Same as (b), now with the intensity of the EEL spectra integrated over the indicated energy windows, also highlighted as vertical grey bands in (b), where intensity enhancements are observed. A black curve indicates the boundary of the nanostructure, and we filter out the substrate. Each panel uses a different intensity range.

at 8.3 eV can be attributed to a plasmonic resonance.[29] For the latter case, an enhancement around 8.3 eV is observed in the inner region of the 1D-MoS$_2$ nanostructures across all the analyzed structures, in alignment with previous reports on plasmonic resonances in 2D-MoS$_2$ nanosheets.[29]
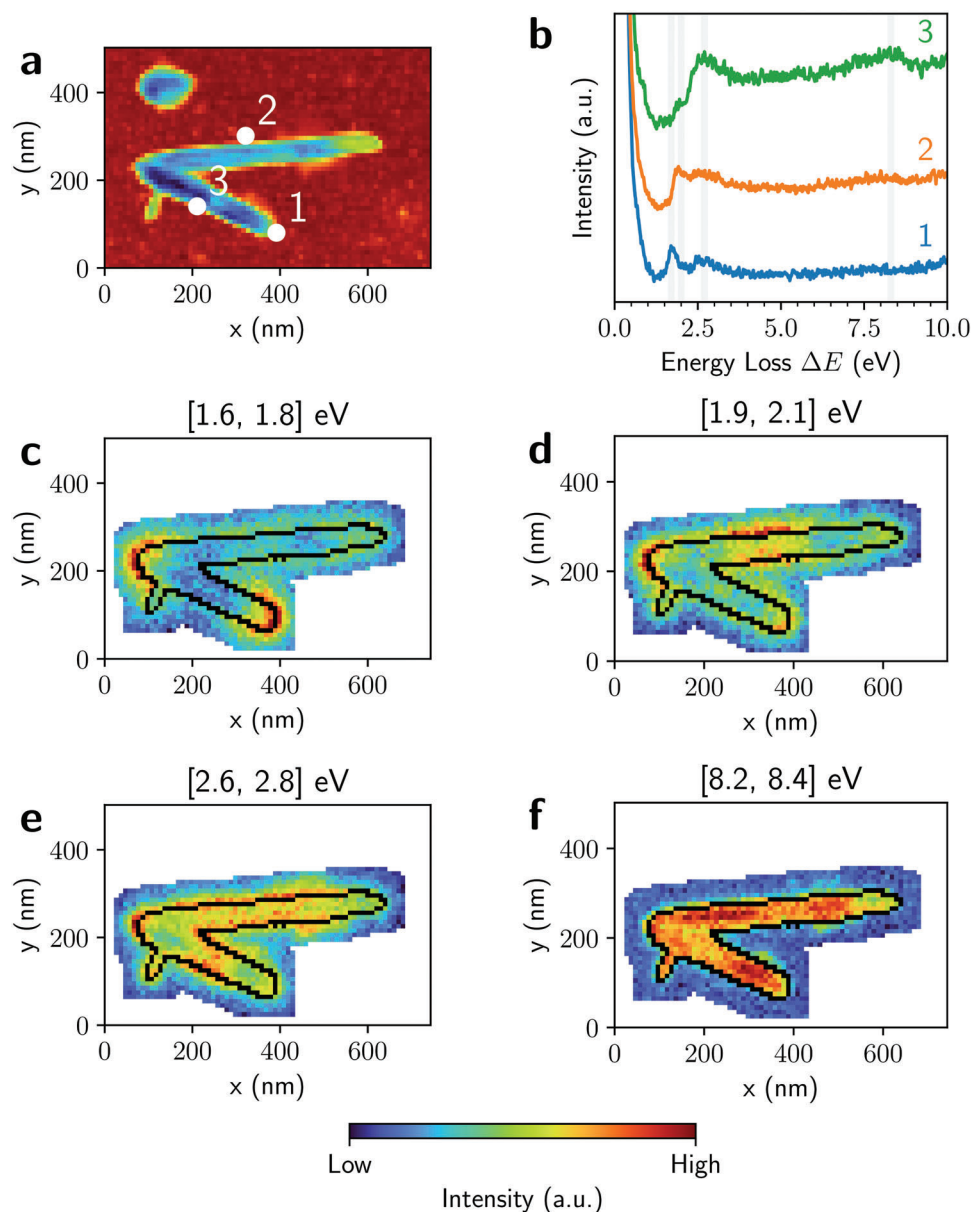
The main differences between our findings on 1D-MoS$_2$ nanostructures and previous investigations on the 2D configuration are summarized by the spatially-resolved analyses of Figures 3 and 4, as well as in Figure S5 (Supporting Information), which establish their correlation with specific locations in the specimen. In contrast with results on 2D-MoS$_2$ nanosheets, where intensity enhancements are typically observed at the edge regions,[29] we find that the enhancements around 2 and 3 eV are localized at either end of the 1D-MoS$_2$ nanostructures (Figures 4c; Figure S5c, Supporting Information) or along their lateral sides (Figures 3d and 4d; Figure S5d, Supporting Information). The fact that these peaks are associated to excitonic transitions[29] and that our analysis indicates that these are restricted to specific regions in the 1D-MoS$_2$ nanostructures ap-

pears to indicate that the observed signals can be associated to spatially-confined MoS$_2$ excitons.

The origin of the peaks observed around 2.7 and 3.0 eV in Figures 4b and Figure S5b (Supporting Information) and (see also Figures 4e; Figure S5d,e, Supporting Information) therefore admits a common origin. Indeed, as previously reported,[29] the enhancement observed at around 3 eV can experience an energy downshift and exhibit a tail extending up to 3.5 eV, consistent with our observations. Furthermore, the intensity distribution across the specimen in the energy intervals around 2.7 and 3.0 eV demonstrates a similar pattern, as displayed in Figures S5d,e (Supporting Information).

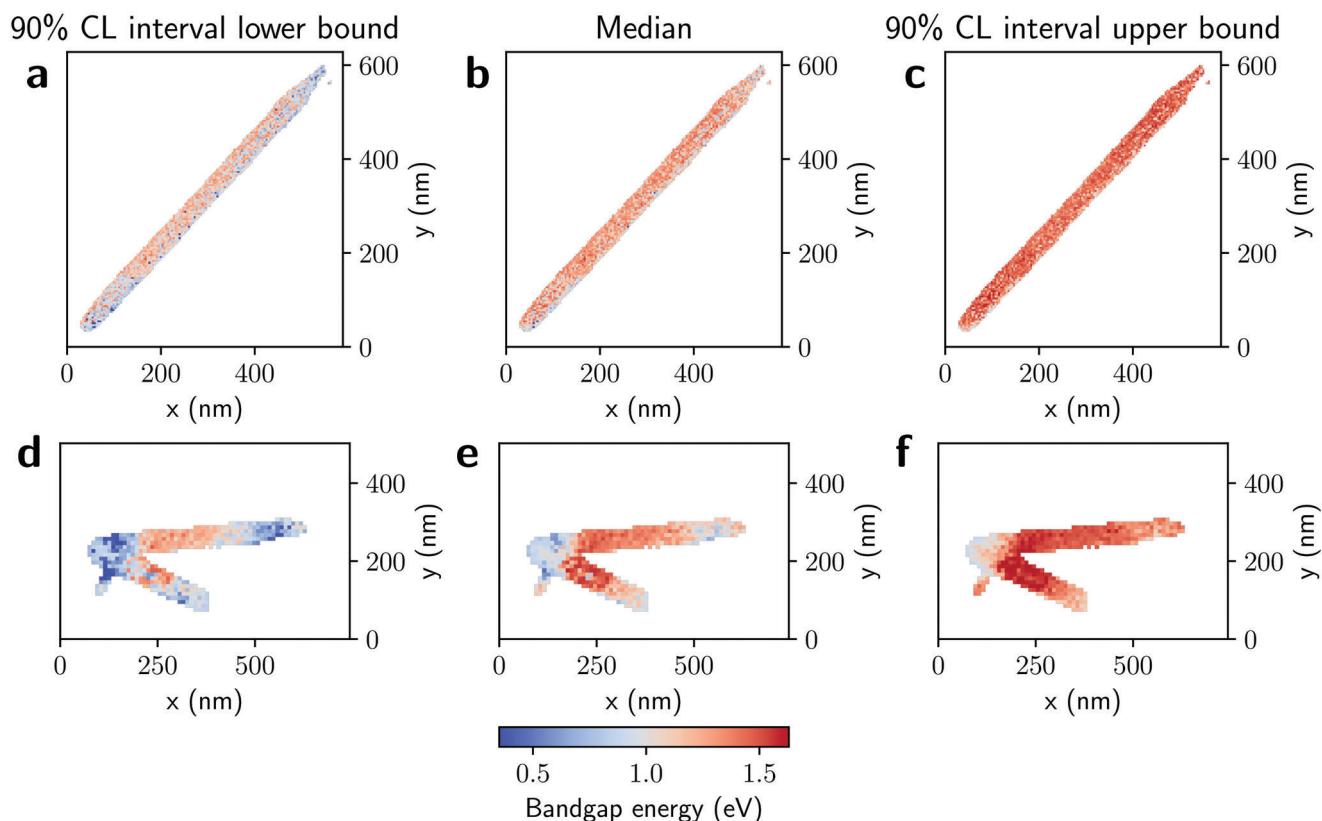## 2.2. Spatially-Resolved Band Gap Energy of 1D-MoS$_2$ Nanostructures

Complementary insights on the local electronic properties of the 1D-MoS$_2$ nanostructures are provided by the spatial distribution

**ADVANCED
SCIENCE NEWS**

www.advancedsciencenews.com

**ADVANCED
FUNCTIONAL
MATERIALS**

www.afm-journal.de

Figure 4. Spatially-resolved EELS analysis of connected 1D-MoS$_2$ nanostructures. Same as Figure 3 now for two 1D-MoS$_2$ nanostructures, with a length of 540 nm and a diameter of 57 nm (top), and a length of 336 nm and a diameter of 62 nm (bottom) respectively, connected by their ends. The corresponding HAADF-STEM image is provided in Figure S2a (Supporting Information).

of their bandgap energy E_{bg}. Here spatially-revolved maps of E_{bg} are determined by analyzing individual EEL spectra after subtracting the ZLP background, following the procedure in [15, 16] and summarized for completeness in Section S4 and S5 (Supporting Information). **Figure 5** displays the E_{bg} maps associated to the 1D-MoS$_2$ nanostructures studied in Figures 3 (individual) and 4 (connected). The first and third columns display the lower (upper) bound of the 90% CL interval for E_{bg}, while the second displays the median. The corresponding bandgap analysis for the specimen analyzed in the Supporting Information are collected in Section S6 (Supporting Information) For all specimens considered, we obtain an indirect bandgap.

The spatially resolved maps of Figure 5 enable identifying correlations between the E_{bg} sensitivity and specific structural features. On the one hand, in the central region of the nanostructures the median E_{bg} is approximately 1.2 eV, consistent with previous findings for bulk MoS$_2$.[34,35] On the other hand, one observes how the values of E_{bg} tend to decrease, as compared to the central region, in the endpoint regions and in the connection region for the joint nanostructure. To quantify this trend, we evaluate in **Table 1** the weighted average bandgap energy in distinct regions within each nanostructure. Specifically, we define the endpoint regions as 20% of the total length of the 1D-MoS$_2$ nanostructures with the central region given by the remaining 60%. This analysis confirms that E_{bg} is reduced in the endpoint

ADVANCED
SCIENCE NEWS
www.advancedsciencenews.com

ADVANCED
FUNCTIONAL
MATERIALS
www.afm-journal.de

Figure 5. Spatially-resolved band gap energy in 1D-MoS$_2$ nanostructures. The median value (second column) and 90% CL lower and upper bounds (first and third column, respectively) for the bandgap energy E_{bg} determined across the 1D-MoS$_2$ nanostructures considered in Figures 3 (top) and 4 (bottom).

Table 1. The weighted average for E_{bg} (in eV) for the 1D-MoS$_2$ nanostructures analyzed in Figure 5, separated into three regions: the left-most endpoint (20% of the total length of the nanostructure), the central region (60%), and right-most endpoint (20%). We also indicate the uncertainty obtained from the 90% CL interval for the weighted average band gap energy.

Specimen	Left-most endpoint	Central region	Right-most endpoint
Figure 3	1.2 ± 0.2	1.3 ± 0.1	1.2 ± 0.2
Figure 4 (bottom)	0.8 ± 0.1	1.1 ± 0.3	1.0 ± 0.2
Figure 4 (top)	0.8 ± 0.2	1.2 ± 0.2	1.0 ± 0.3

regions as compared to the central ones. The statistical significance of this bandgap energy variation is found to be between the 1σ and 2σ level, depending on the nanostructure.

A possible explanation of this trend is provided by the presence of curvature-induced local strain identified in Figure 2b,c, e,f in the endpoint and in the lateral regions, respectively, which has been reported to modify the bandgap energy. The relative decrease of E_{bg} observed in regions with tensile strain at the level quantified in Figure 2 is consistent, within uncertainties, with previous reports on 2D-MoS$_2$.[36,37]

Local strain is also known to induce a downshift in the excitonic transition energies.[38,39] We verify in Section S7 (Supporting Information), which analyzes the modulation of the 1.9 eV

exciton peak location across the specimen, that indeed a downshift between 3% and 4% is obtained in our 1D-MoS$_2$ specimens. The decrease in the bandgap energy E_{bg} in the endpoint regions of the 1D-MoS$_2$ nanostructures as compared to the central region may hence be attributed to curvature-induced local strain fields, which in turn is consistent with the observed exciton localization pattern.

2.3. Summary and Outlook

Our investigation of the electronic and structural characteristics of 1D-MoS$_2$ nanostructures has resulted into several key insights. First, we observed excitonic transitions localized at either the endpoints or the lateral sides of the nanostructures, particularly around energy losses of 2 and 3 eV, at odds with the case of 2D-MoS$_2$ materials where the analogous intensity enhancements are typically observed across the structure. Second, our studies identifies the presence of plasmonic resonances localized at 8.3 eV in the inner region of the 1D-MoS$_2$ nanostructures, aligning with previous observations in 2D-MoS$_2$. Thirdly, we have quantified the spatial modulation of the bandgap energy across the 1D-MoS$_2$ nanostructures, finding that the endpoint regions display a decreased bandgap as compared to the bulk MoS$_2$ value due to the presence of curvature-induced local strain effects. The same

curvature-driven strain fields are likely to be responsible for the localization of the confined excitonic transitions observed.

Our results underscore the rich diversity of electronic behaviors in 1D-MoS_2 nanostructures and highlight the potential for tailoring these properties for specific applications by engineering the nanostructure's morphology and spatial configuration. In particular, they showcase the potential of curvature-induced strain as a useful handle to tune optoelectronic properties. This strain-dependent modulation of the bandgap energy in 1D-MoS_2 nanostructures could be leveraged in strain-engineered optoelectronic devices, while being able to reproducibly generate strain-confined excitons, opens new avenues for single-photon emitters to be used in quantum optics and quantum networks.

3. Experimental Section

Synthesis of the 1D-MoS_2 Nanostructures: The 1D-MoS_2 nanostructures were synthesized using CVD on a TEM grid. The TEM grid used in this study consisted of nine viewing windows with a Si_3N_4 thin film spanning across the entire grid (EMS Catalog #76042). To initiate the synthesis, a small amount of MoO_2 (99 %, Sigma–Aldrich 234761) was drop-casted onto the TEM grid. This involved using a solution containing 2.6 mg of MoO_2 suspended in 6 ml of isopropanol. The grid, with the MoO_2 precursor, was then positioned in an alumina crucible, approximately 2 cm away from 7.5 mg of MoO_2 powder.

The experimental setup included a gradient tube furnace from Carbolite Gero, with the alumina crucible placed in the middle of the furnace. Upstream from this crucible, another alumina crucible contained 400 mg of sulfur (99.5 %, Alfa Aesar 10785). Throughout the synthesis process, argon was used as a carrier gas at a flow rate of 100 sccm. The middle zone of the furnace was heated to 780 °C, while the sulfur reached a maximum temperature of 270 °C. It is noteworthy that a small fraction of the resulting nanostructures exhibited MoO_3 cores instead of MoS_2. This indicates that the sulfurization process was not fully completed for these particular nanostructures. Additionally, it was observed that the MoO_2 powder used as a seed material during the synthesis underwent a conversion to MoO_3. The confirmation of this conversion from MoO_2 to MoO_3 was achieved trough the mapping of the bulk plasmon characteristic of MoO_3. This analysis is depicted in Figure S3 (Supporting Information). This growth procedure results into 1D-MoS_2 nanostructures exhibiting the 2H crystal phase.

Supporting Information

Supporting Information is available from the Wiley Online Library or from the author.

Acknowledgements

Author Contributions

S.C.-B. conducted experiments and collected data. S.v.d.L. and A.B. worked on the code and the user interface for the EELS analysis. S.v.d.L. and A.B. conducted data analysis and interpretation of EELS measurements, with input from J.t.H., J.R., and S.C-B. S.C.-B. conducted the GPA analysis. S.v.d.L. and S.C.-B. were responsible for writing the initial draft of the manuscript, with input and revisions from all authors. All authors contributed to reviewing and editing the manuscript. All authors had read and approved the final version of the manuscript. S.C.-B supervised all aspects of the project.

Conflict of Interest

The authors declare no conflict of interest.

Data Availability Statement

The data that support the findings of this study are available from the corresponding author upon reasonable request.

Keywords

[1] P. H. López, S. Heeg, C. Schattauer, S. Kovalchuk, A. Kumar, D. J. Bock, J. N. Kirchhof, B. Höfer, K. Greben, D. Yagodkin, L. Linhart, F. Libisch, K. I. Bolotin, *Nat. Commun.* **2022**, *13*, 7691.

[2] S. Zhang, C.-G. Wang, M.-Y. Li, D. Huang, L.-J. Li, W. Ji, S. Wu, *Phys. Rev. Lett.* **2017**, *119*, 046101.

[3] Y. J. Zheng, Y. Chen, Y. L. Huang, P. K. Gogoi, M.-Y. Li, L.-J. Li, P. E. Trevisanutto, Q. Wang, S. J. Pennycook, A. T. S. Wee, S. Y. Quek, *ACS Nano* **2019**, *13*, 6050.

[4] H. Li, A. W. Contryman, X. Qian, S. M. Ardakani, Y. Gong, X. Wang, J. M. Weisse, C. H. Lee, J. Zhao, P. M. Ajayan, J. Li, H. C. Manoharan, X. Zheng, *Nat. Commun.* **2015**, *6*, 1.

[5] T. P. Darlington, C. Carmesin, M. Florian, E. Yanev, O. Ajayi, J. Ardelean, D. A. Rhodes, A. Ghiotto, A. Krayev, K. Watanabe, T. Taniguchi, J. W. Kysar, A. N. Pasupathy, J. C. Hone, F. Jahnke, N. J. Borys, P. J. Schuck, *Nat. Nanotechnol.* **2020**, *15*, 854.

[6] C. Chakraborty, L. Kinnischtzke, K. M. Goodfellow, R. Beams, A. N. Vamivakas, *Nat. Nanotechnol.* **2015**, *10*, 507.

[7] G. Moody, K. Tran, X. Lu, T. Autry, J. M. Fraser, R. P. Mirin, L. Yang, X. Li, K. L. Silverman, *Phys. Rev. Lett.* **2018**, *121*, 057403.

[8] I. Niehues, R. Schmidt, M. Drüppel, P. Marauhn, D. Christiansen, M. Selig, G. Berghäuser, R. Wigger, R. Schneider, L. Braasch, R. Koch, A. Castellanos-Gomez, T. Kuhn, A. Knorr, E. Malic, M. Rohlfing, S. M. de Vasconcellos, R. Bratschitsch, *Nano Lett.* **2018**, *18*, 1751.

[9] S. Kumar, A. Kaczmarczyk, B. D. Gerardot, *ACS Publ.* **2015**, *15*, 7567.

[10] Q. Wang, J. Maisch, F. Tang, D. Zhao, S. Yang, R. Joos, S. L. Portalupi, P. Michler, J. H. Smet, *Nano Lett.* **2021**, *21*, 7175.

[11] I. Aharonovich, D. Englund, M. Toth, *Nat. Photonics* **2016**, *10*, 631.

[12] *Quantum Dots for Quantum Information Technologies*, Springer International Publishing, Cham, Switzerland **2017**.

[13] H. J. Kimble, *Nature* **2008**, *453*, 1023.

[14] Y.-M. He, G. Clark, J. R. Schaibley, Y. He, M.-C. Chen, Y.-J. Wei, X. Ding, Q. Zhang, W. Yao, X. Xu, C.-Y. Lu, J.-W. Pan, *Nat. Nanotechnol.* **2015**, *10*, 497.

**ADVANCED
SCIENCE NEWS**

www.advancedsciencenews.com

**ADVANCED
FUNCTIONAL
MATERIALS**

www.afm-journal.de

[15] L. I. Roest, S. E. van Heijst, L. Maduro, J. Rojo, S. Conesa-Boj, *Ultramicroscopy* **2021**, *222*, 113202.

[16] A. Brokkelkamp, J. ter Hoeve, I. Postmes, S. E. van Heijst, L. Maduro, A. V. Davydov, S. Krylyuk, J. Rojo, S. Conesa-Boj, *J. Phys. Chem. A* **2022**, *126*, 1255.

[17] M. Bolhuis, J. Hernandez-Rueda, S. E. van Heijst, M. Tinoco Rivas, L. Kuipers, S. Conesa-Boj, *Nanoscale* **2020**, *12*, 10491.

[18] M. Tinoco, L. Maduro, S. Conesa-Boj, *Sci. Rep.* **2019**, *9*, 15602.

[19] B. Yue, F. Hong, K.-D. Tsuei, N. Hiraoka, Y.-H. Wu, V. M. Silkin, B. Chen, H.-k. Mao, *Phys. Rev. B* **2017**, *96*, 125118.

[20] L. Martin, R. Mamy, A. Couget, C. Raisin, *Phys. Status Solidi B* **1973**, *58*, 623.

[21] K. Zeppenfeld, *Opt. Commun.* **1970**, *1*, 377.

[22] W. Y. Liang, S. L. Cundy, *Philos. Mag.: A J. Theor. Exper. Appl. Phys.* **1969**, *19*, 1031.

[23] A. Splendiani, L. Sun, Y. Zhang, T. Li, J. Kim, C.-Y. Chim, G. Galli, F. Wang, *Nano Lett.* **2010**, *10*, 1271.

[24] J. Rouvière, E. Sarigiannidou, *Ultramicroscopy* **2005**, *106*, 1.

[25] M. Tinoco, L. Maduro, M. Masaki, E. Okunishi, S. Conesa-Boj, *Nano Lett.* **2017**, *17*, 7021.

[26] A. P. Rooney, Z. Li, W. Zhao, A. Gholinia, A. Kozikov, G. Auton, F. Ding, R. V. Gorbachev, R. J. Young, S. J. Haigh, *Nat. Commun.* **2018**, *9*, 3597.

[27] N. Grobert, M. Mayne, M. Terrones, J. Sloan, R. E. Dunin-Borkowski, R. Kamalakaran, T. Seeger, H. Terrones, M. Rühle, D. R. M. Walton, H. W. Kroto, J. L. Hutchison, *AIP Conf. Proc.* **2001**, *591*, 287.

[28] J. Sloan, J. L. Hutchison, R. Tenne, Y. Feldman, T. Tsirlina, M. Homyonfer, *J. Solid State Chem.* **1999**, *144*, 100.

[29] H. C. Nerl, K. T. Winther, F. S. Hage, K. S. Thygesen, L. Houben, C. Backes, J. N. Coleman, Q. M. Ramasse, V. Nicolosi, *npj 2D Mater. Appl.* **2017**, *1*, 2.

[30] A. Molina-Sánchez, D. Sangalli, K. Hummer, A. Marini, L. Wirtz, *Phys. Rev. B* **2013**, *88*, 045412.

[31] L. H. G. Tizei, Y.-C. Lin, M. Mukai, H. Sawada, A.-Y. Lu, L.-J. Li, K. Kimoto, K. Suenaga, *Phys. Rev. Lett.* **2015**, *114*, 107601.

[32] X. Sui, H. Wang, C. Liang, Q. Zhang, H. Bo, K. Wu, Z. Zhu, Y. Gong, S. Yue, H. Chen, Q. Shang, Y. Mi, P. Gao, Y. Zhang, S. Meng, X. Liu, *Nano Lett.* **2022**, *22*, 5651.

[33] X. Hong, J. Kim, S.-F. Shi, Y. Zhang, C. Jin, Y. Sun, S. Tongay, J. Wu, Y. Zhang, F. Wang, *Nat. Nanotechnol.* **2014**, *9*, 682.

[34] K. K. Kam, B. A. Parkinson, *J. Phys. Chem.* **1982**, *86*, 463.

[35] J. Gusakova, X. Wang, L. L. Shiau, A. Krivosheeva, V. Shaposhnikov, V. Borisenko, V. Gusakov, B. K. Tay, *Phys. Status Solidi A* **2017**, *214*, 1700218.

[36] Z. Peng, X. Chen, Y. Fan, D. J. Srolovitz, D. Lei, *Light Sci. Appl.* **2020**, *9*, 1.

[37] H. J. Conley, B. Wang, J. I. Ziegler, R. F. Haglund, Jr, S. T. Pantelides, K. I. Bolotin, *Nano Lett.* **2013**, *13*, 3626.

[38] M. Tinoco, L. Maduro, M. Masaki, E. Okunishi, S. Conesa-Boj, *Nano Lett.* **2017**, *17*, 7021.

[39] S. Pak, J. Lee, Y.-W. Lee, A.-R. Jang, S. Ahn, K. Y. Ma, Y. Cho, J. Hong, S. Lee, H. Y. Jeong, H. Im, H. S. Shin, S. M. Morris, S. Cha, J. I. Sohn, J. M. Kim, *Nano Lett.* **2017**, *17*, 5634.